

# DESIGN PROCESS AND MANUFACTURING OF AN UNMANNED BLENDED WING-BODY AIRCRAFT

Benjamin Gramüller\*, Felix Stroscher\*\*, Jochen Schmidt\*, Tanut Ungwattapanit\*\*, Thomas Löbel\*, Michael Hanke\*

## Abstract:

The design process, the dimensioning, the proof and the manufacturing of a blended wing-body configuration aircraft with diamond shape is presented. The open collaboration project *Sagitta* is initiated by *Airbus Defence and Space* with the objective to investigate innovative aircraft configurations for future unmanned aerial systems (UAS) and the therefor necessary technologies. In cooperation of the *German Aerospace Centre* (DLR) and the *Technical University of Munich* (TUM) the aircraft structure is realized. A brief project overview points out the objectives of *Sagitta* and summarizes the characteristics of the extremely lightweight carbon fibre structure. This work focusses on the computation of loads, the process of structural sizing, the simulation-based mainly structural proof and the manufacturing. Particular attention is paid to the specifically developed semi-analytical method for dimensioning adhesive joints. Basing on the detailed finite element model of the global structure, the applicability of adhesive joints as major structural joining variant is proven. The manufacturing process from single components to the assembly of the overall aircraft concludes the realization of the *Sagitta* demonstrator structure.

## 1 Project and system overview

Various studies like *ETAP GSS*, *Air4All* and *UCAS2020+* identified a broad spectrum of gaps regarding unmanned aerial vehicle (UAV) technology in Europe. Major topics in this field are

- high degree of autonomy,
- advanced sensor package and information fusion,
- long range & extended loiter time,
- sophisticated covert communication and
- low observable (LO) & effective self-defence suite.

*Sagitta* is initiated by *Airbus Defence and Space* as German research collaboration for UAS technology between mainly academy institutions. It is separated into a research program and the implementation and operation of a research demonstrator. The realization of a scaled aircraft with a wingspan of about three meters serves as platform for demonstrating research technologies in the fields of preliminary aircraft design, aerodynamics [1], flight control systems, communications and data processing, vision-based flight control and air-to-air refueling, materials and structure, autonomous flight and mission control [2]. The downscaled (1:4) demonstrator is based on a future low observable UAV configuration and is depicted in Figure 1. The maximum take-off mass is limited to 150 kg to be free of certification for operation in a restricted airspace. Two internal jet engines provide 300 N of thrust each. The design flight time is about one hour with flight speeds between  $v_{min} = 35 \text{ m/s}$  and  $v_{max} = 100 \text{ m/s}$ . The structure of the aircraft is mainly designed of carbon fibre reinforced plastic (CFRP). Few

metallic parts are utilized where appropriate (e.g. heatshield, landing gear).

The starting point for structural design is the aerodynamically dominated hull geometry. The leading edge is shaped sharp at the nose and fades into rounded shape for increased span. On the basis of aerodynamic studies a control surface layout is integrated into the hull geometry. From inboard to outboard, the trailing edge is separated into an exhaust section, elevators, ailerons and outboard split flaps for yaw control.

In the preliminary design phase multiple designs for the structure are conceived. The following influencing factors and basic requirements are mainly responsible for the decision that led to the selected design. The structural concept shall

- withstand external and internal loads,
- carry propulsion, electronic and termination systems,
- ensure a high grade of manoeuvrability,
- be extremely lightweight,
- enable a low radar cross section and
- fulfil the requirements of a full-scale UAV.

The different concepts are evaluated by structural analysis including preliminary flight loads. Figure 2 outlines the considered configurations and shows the final structural layout in the lower part of the figure. Key features of the final concept are

- discrete load paths built by spars, ribs and belts,
- monocoque construction for skin and covers and
- large free space for extensive mission and flight equipment.

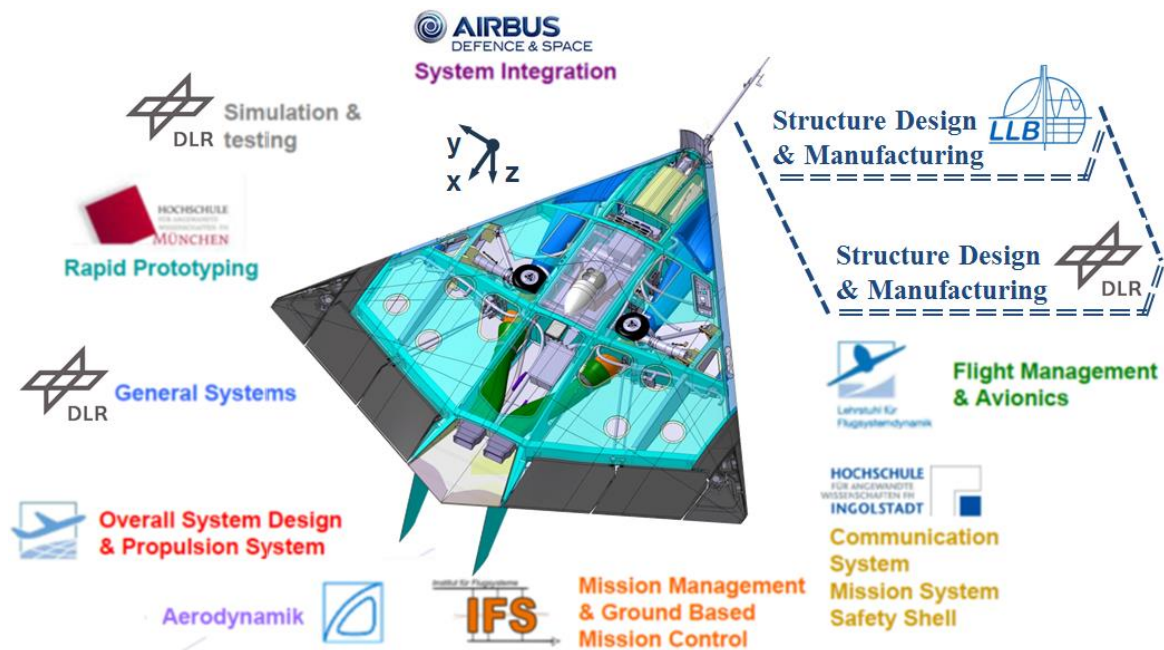


Figure 1: Project and Systems Overview

## 2 Loads analysis

The structural integrity of the *Sagitta* demonstrator has to be proven for all identified load situations. These can be characterized by the following quasi-static external loads:

Alternative structural design concepts

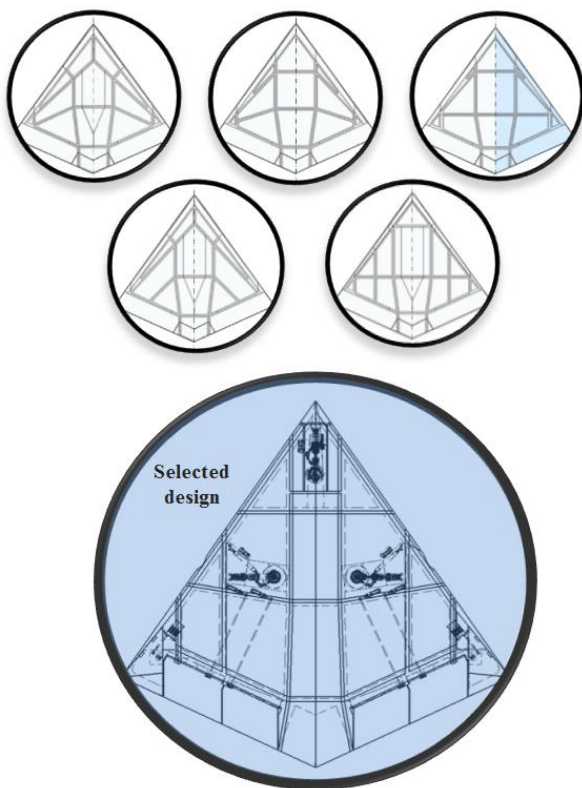


Figure 2: Selection of preliminary design concept for providing geometrical and weight efficient load paths based on the numerical evaluation of discrete design alternatives

- Ground operations
- Flight maneuvers
- Landing
- Termination in flight
- Actuator stall loads
- Flutter

Additionally to quasi-static external loads, the aeroelastic stability analysis ensures the integrity of the structure due to dynamic effects.

### 2.1 External quasi-static loads

For consideration of Ultimate Loads all external quasi-static loads need to be applied with a safety factor of 1.5, except the termination loads, which is a failure load case. For any of the given situations, the aircraft is considered in free flight. Thus no displacement boundary condition is applied. Inertial loads are accounted by inertia relief computation, such that the sum of inertial and external forces is in balance.

#### 2.1.1 Landing loads

The loads on the *a/c* at landing operation are predicted by dynamic multi body simulation. For this purpose, a simulation model is built in *Matlab Simulink*, representing the airframe as a rigid body and landing gears as nonlinear spring-damper systems. The landing operation is simulated in time domain for all possible combinations of approach speed, wind speed, roll, pitch and yaw angle. The static landing load cases are derived from time histories of forces and moments at the upper end of the spring-damper systems. This load transfer point is used as interface between the landing simulation model and the

structural analysis model. In order to find most critical load cases, the maxima of each individual load direction are identified. The static load case is then composed from the complete load vector of these points at the specific time.

This approach neglects dynamic response of the structure during landing. However, as the supporting structure for the landing gear is relatively stiff, this error is considered low and covered by the load safety factor of 1.5.

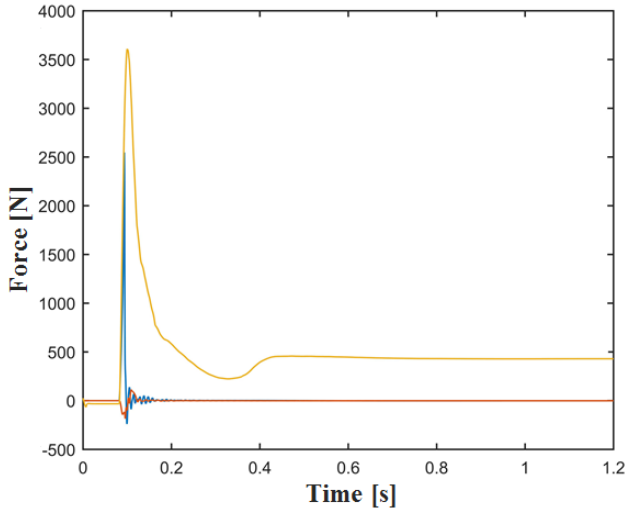


**Figure 3: Force progression over time of right main landing gear at the structural interface**

### 2.1.2 Manoeuvre loads

The static structural response from manoeuvring is part of the structural proof. An ultimate load factor of 1.5 is applied for manoeuvre Ultimate Loads. The stress and buckling response is computed by static aeroelastic analysis of the finite element model, which is coupled to a separate panel model (see Figure 4) for computation of steady aerodynamic loads. The *Doublet Lattice Method* is applied as aerodynamic theory.

The vertical load factor envelope of the *Sagitta* demonstrator is given to  $\pm 5g$ , combined with lateral dynamic flight conditions.

### 2.1.3 Gust loads

The aircraft is designed to discrete gust loads in accordance to CS 23.341, assuming a minimum flight design weight of 100 kg. Discrete gust loads are computed by dynamic aeroelastic analysis in *MSC Nastran*. Symmetrical vertical gusts with the following gust velocities are considered:

- Vertical gust velocity (at  $v_{Cruise} = 80 m/s$ , sea level) of 50 fps as Limit Load
- Vertical gust velocity (at  $v_{Dive} = 100 m/s$ , sea level) of 25 fps as Limit Load

The incremental gust load factors at the centre of gravity and at the wingtip are computed for cruise speeds between  $v_{min}$  and  $v_{max}$ . The total load factor  $n$  at discrete gust incident is derived by adding 1 g to the incremental

gust load factor and results in  $n_{WingTip} = 10.2$  and  $n_{C.G.} = 9.0$  for a vertical gust velocity of 50 fps.

### 2.1.4 Termination loads

The maximum load peak to be expected during the opening sequence of the utilized termination chute *DO-DT 25HD* is 8826N. As no further information is available and the maximum flight speed is limited to 100 m/s, the value for the maximum opening shock is taken from a parachute test flight case at 185 m/s speed. Thus it guarantees a safe dimensioning of attachment and surrounding structure. For sizing the structure to withstand the loads applied by the termination system, seventeen force vectors are used. The vectors are oriented in 45° steps to uniformly cover the complete aircraft-averted hemisphere of the termination system (TRS) opening.

### 2.1.5 Control surface loads

Required for control authority during flight manoeuvres, extreme hinge moments are determined and used to estimate the pressure distribution acting on corresponding control surfaces. The following circumstances are considered:

- Extreme hinge momentums from aerodynamic loads while actuation mechanism is fixed
- Extreme hinge moments from actuator stall load
- Extreme inertial loads acting parallel to the hinge line in accordance to CS23.393. Inertial loads equal to 12 times the movable surface weight

A triangular pressure distribution, as shown in Figure 4, is applied on control surfaces and scaled to result into the required hinge moment. The critical hinge momentum results from actuator stall loads for all flaps, which is 12 Nm multiplied by transmission ratio from actuator axis to hinge line.

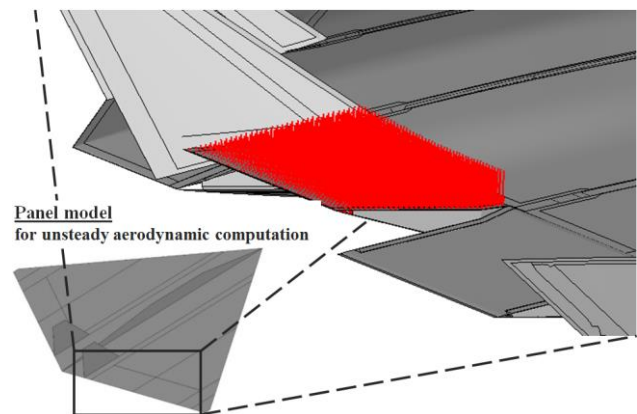


**Figure 4: Load distribution on elevator, based on panel model computations**

## 2.2 Aeroelastic stability

The structure shall be free from flutter and divergence up to 1.2 times its maximum operating speed  $v_{Dive}$ . The

flutter analysis is performed by finite element analysis of the structural dynamics and the *Double Lattice Method* for unsteady aerodynamics, which is based on linear potential theory. A ground vibration test has to be conducted, to verify the structural dynamic modelling.

### 3 Structural Sizing

The design criteria for the sizing process are presented before the sizing model is described. The sizing of the structure is based on the preliminary design concept (cf. Figure 2). The therein determined shape, position and orientation of spars, ribs and major attachments, for the landing gear, the termination system and the flaps, provide the necessary input for the creation of the sizing model. Information about the iterative process of sizing using *HyperSizer* is given before the results are summarized.

#### 3.1 Design criteria

The structure of the Sagitta demonstrator is designed to fulfil the requirements of LTF1550-001, category 1, however, it will be operated under permission of the responsible authorities according to §15a LuftVO. The critical system for receiving this permission is the TRS, which is based on a termination parachute together with engine fuel cut. It satisfies the requirement not to leave the restricted flight test area.

##### 3.1.1 Static Strength

Static strength criteria are applied for dimensioning the *Sagitta* structure. The structural strength characteristics for the components' materials, like monolithic composite and sandwich, as well as strength specifications for bolted and adhesive joints provide the basis for the subsequent sizing process. The subsequently presented methods and the related characteristic values are used for the sizing of the global structure.

###### 3.1.1.1 Isotropic material

Metal fittings are used for the attachment of flaps and actuators, the landing gear, the termination parachute and electronic components. The *von Mises* criterion is utilized to compute structural equivalent stresses and to evaluate it with the material yield tensile strength. For alloy, the yield strain can be assumed at 0.2 %. The following stress relation is to be complied:

$$(R_{p,0.2}/\sigma_{vM}) - 1 > 0. \quad (1)$$

Where  $R_{p,0.2}$  is the yield tensile strength and  $\sigma_{vM,max}$  is the maximum von Mises stress. The applied materials are

- Aluminum EN AW 7075-T651,
- Steel X5CrNi18-10,
- Steel ETG 100 and

- Titan Ti6Al4V.

##### 3.1.1.2 Composite material

Besides few metal parts, the predominant material, which is used for Sagitta is carbon fibre reinforced plastic (CFRP). The *Maximum Strain* criterion is chosen for the prediction of first-ply failure of the thin-walled composite structures. Its characteristic properties and in particular the elastic moduli of  $E_{qiso} \approx 50 \text{ GPa}$ , for quasi-isotropic and  $E_{UD} \approx 120 \text{ GPa}$ , for unidirectional laminates, together with maximum strain values of  $\chi_{||} \approx 0.36 \dots 0.67$  allow to achieve light-weight and stiffness aims. Structural integrity is given, as long as

$$(\chi_d/|\varepsilon_d|) - 1 > 0 \quad (2)$$

is fulfilled. The structure can withstand the applied loads when the absolute value of the maximum laminae strains  $\varepsilon_d$  with direction  $d$  is less than or equal to the strength value  $\chi_d$ . The computed strains are evaluated in fibre parallel, perpendicular and shear direction. The CFRP materials that are used for Sagitta (cf. Table 1) are restricted to prepreg systems due to manufacturing advantages and weight-saving potentials. Investigations comparing the fibre volume fraction (FVF) of infused and prepreg material components showed that the resin absorption especially in areas of integrally manufactured sandwich material can be reduced with prepreg. Weight-savings can thus be achieved. Moreover, the challenging infusion of huge areas of thin-walled laminates could thus be circumvented.

**Table 1: CFRP prepreg materials utilized for Sagitta structure**

Supplier	Type	Fiber	Resin
Oxeon	Fabric	UTS50	MTC400
Cytec	Fabric	T800	MTM49-3
SHD Composites	UD-tape	T800	MTC400
Cytec	UD-tape	T800	MTM49-3

Figure 5 gives an overview about the material data, which is utilized for the sizing of *Sagitta*. The presented values result from an experimental characterization program, which is complemented by datasheet values and processed for the consideration of the manufacturing-dependent FVF, probabilistic (B-Value) and temperature (Hot/Wet) aspects. The operating temperatures of the aircraft lie between  $T_{min} = -20 \text{ }^\circ\text{C}$  and  $T_{max} = 70 \text{ }^\circ\text{C}$ .




UTS50, MTC400 (fabric)	T800, MTM49-3 (fabric)	UTS50, MTC400 (UD) T800, MTM49-3 (UD)
→ Skin shells	→ Inner structure	→ Belts
		
$E_t = 59 \text{ GPa}$ $E_c = 51 \text{ GPa}$ $\varepsilon_t = 6860 \text{ }\mu\text{m/m}$ $\varepsilon_c = 4370 \text{ }\mu\text{m/m}$  FVF = 50.34 % $\rho = 1.45 \text{ t/m}^3$	$E_t = 70 \text{ GPa}$ $E_c = 62 \text{ GPa}$ $\varepsilon_t = 5410 \text{ }\mu\text{m/m}$ $\varepsilon_c = 3680 \text{ }\mu\text{m/m}$  FVF = 55.0 % $\rho = 1.50 \text{ t/m}^3$	$E_{11} = 135 \text{ GPa}$ $E_{22} = 8 \text{ GPa}$ $\varepsilon_{11} = 5620 \text{ }\mu\text{m/m}$ $\varepsilon_{22} = 4880 \text{ }\mu\text{m/m}$  FVF = 55.0 % $\rho = 1.50 \text{ t/m}^3$

Figure 5: Excerpt of the CFRP material data

### 3.1.1.3 Sandwich material

Thin-walled CFRP structures are well suited for stiffening webs and skins against tensional loads in surface parallel direction. Buckling, as a result of compressive in-plane forces or out-of-plane forces, can be avoided by using sandwich structures. The increased geometrical moment of inertia compared to monolithic variants of equal mass, allows preventing buckling.

Sandwich structures further must be dimensioned to withstand the following types of loads (detailed analytical methods are given in [3]):

- Sandwich flatwise tension, top/bottom foam face
- Foam core crushing

Four polymethacrylimide (PMI) foams with different densities are utilized as sandwich core. The selection depends on the locally occurring loads. The characteristic stiffness and strength values of the foam core and face material determine the bearable loads. All of the applied foam cores are taken from the product series *Rohacell* of *Evonik Industries* and are named

- Rohacell 51 IGF,
- Rohacell 51 RIMA,
- Rohacell 71 IGF and
- Rohacell 71 RIMA.

### 3.1.1.4 Bolted and adhesive joints

The dimensioning and structural proof of bolted and adhesive joints bases on the outcomes of the numerical investigations utilizing the detailed finite element method (FEM) model, which is presented in chapter 4. The sizing procedure focusses on the design of structural components. The necessary level of detail regarding the components' geometry and the load introduction for the analysis of joints is not available at that state of the project. The related methods are given in chapter 4.1.

### 3.1.2 Stability

The sandwich panels as well as the monolithic isotropic, CFRP structures are dimensioned to prevent buckling. Wrinkling for the top and bottom foam face is considered

for the dimensioning of sandwich structures. Analytical methods are used within the *HyperSizer* optimization tool to compute effective stiffness and area of complex shaped surfaces and to evaluate the safety factors with respect to buckling. The underlying methods are given in [3].

## 3.2 Description of sizing model

The geometry that is used for the FEM calculations consists of two skin shells, spars, ribs, attachments for wing tip, landing gear, flaps, and termination system, as well as of a dummy structure for the landing gear and the vertical tails. It is deduced from the preliminary CAD surface model. The preprocessing tool *MSC Patran* is utilized for this purpose. Ultimate Loads, presented in chapter 2, are applied to the model in terms of separate load data files. Boundary conditions are substituted by inertia relief conditions. Drap simulation is processed with the *Laminate Modeler* and allows considering variations of the fiber angles due to the application on double-curved surfaces. The mean element size is  $10 \times 10 \text{ mm}^2$ . This value is manually adjusted to decrease in areas of high strain gradients.

The FEM model, depicted in Figure 6, primarily consists of *Quad4* and *Tria3* shell elements, which are used for thin-walled components and sandwich sections. Landing gear, flap actuation rods and vertical tail are modelled with *Bar2* bar elements. The rigid body elements *RBE2* and *RBE3* are used for connecting jointed components, modelling kinematics and applying forces. *Glued Contact* allows connecting the landing gear and termination system attachments to the underlying structure. This rigid linkage is replaced by solid elements in the more detailed structural proof model. The stiffness of the utilized adhesive and shim material is thus considered.

The FEM model, which includes geometry, mesh, load cases and initial properties, provides the main input for the sizing model. The sizing relevant information like load factors, materials, ply and laminate thickness constraints, laminate stacking rules, definition of sections and its bearing complete the data set, which is needed for the optimization. The sizing tool *HyperSizer* offers an appropriate software environment for this input.

## 3.3 Sizing process using HyperSizer

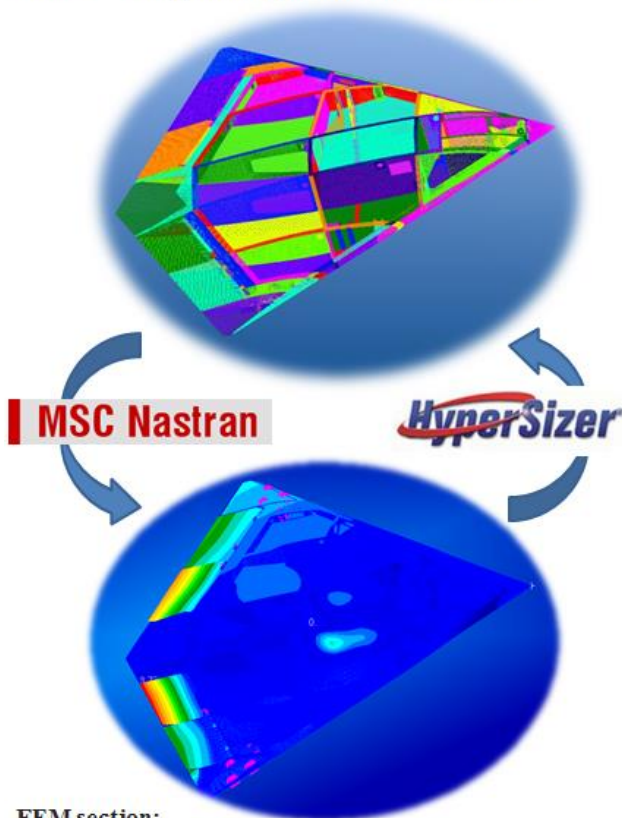
*HyperSizer* uses a semi-analytical iterative process to calculate an optimal material allocation for multiple sizing sections at macroscopic considerations. The sizing procedure can be applied for single panels or components or for global structures with hundreds of property sections and shall be described in the following.

The software on its own is not able to perform a complete sizing step. For each iteration step an external FEM solver, in this case *MSC Nastran*, provides the capabilities of solving the FEM model. The computational results and in particular the element forces are extracted to evaluate the available strength and stiffness properties of the sizing sections in the following. At this point the actual sizing is initiated. Analytical methods establish the link between

the numerically computed section loads and the necessary material application that is needed for bearing it and to fulfil stability criteria. The adaption of the properties towards a mass minimum causes a redistribution of loads in the global structure and thus alters the global load distribution.

**Sizing section:**

**Objectives:** Definition of property sections  
 Optimization of property  
 Model update  
**Software:** HyperSizer  
**Input:** Load distribution (element forces)  
**Results:** Sizing according to current load distribution



**FEM section:**

**Objectives:** Solving of FEM-model  
 Computation of load distribution  
**Software:** MSC Nastran  
**Input:** Geometry and mesh  
 Load and boundary conditions  
 Properties  
**Results:** Load distribution

**Figure 6: Sizing model of Sagitta with varying colours for each individually optimized structural section and iterative process of calculating structural loads and optimizing section properties**

An iterative process is utilized to provide remedy. Figure 6 shows this process, the sizing model and the structural deformations for a single load case. A feasible solution for the structural properties is found, when the change of properties and thus the related change of load flow vanishes.

Subsequently to the sizing procedure, a manufacturing optimization tool provides the possibility to consider boundary conditions for the laminate design. The first optimization process bases on so-called effective

laminates. Without considering material and manufacturing boundary conditions arbitrary laminate thicknesses can be applied to the property sections. In a second step these effective laminates are transferred to discrete laminates. The ply thickness, stacking rules and the stacking sequence regarding ply drops can be considered in this discretization. The iteration-based process, as depicted in Figure 6, again allows taking load redistribution into account.

For Sagitta, 316 individually modified sizing sections are defined. With a set of four CFRP and four foam core materials the laminate and sandwich layup for these sections is calculated under consideration of 157 load cases.

**3.4 Sizing results**

The structure is sized to fulfil the requirements of strength and stability. The weight development as an indicator for the convergence of the process is presented in Figure 7. After the definition of an arbitrary initial property, which is needed to calculate a first load distribution the total mass converges for an increasing number of iterations. As effective laminates do not rely on stacking rules and ply thicknesses, an increase of weight comes along with the discretization of laminates. The final mass of 19.46 kg results for the structure and does not include fasteners, attachments, adhesives and paint.

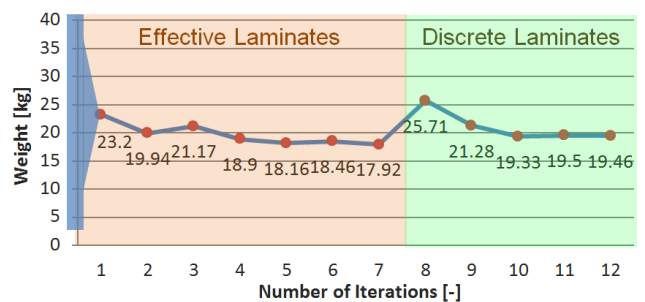


**Figure 7: Global weight development for increasing number of sizing steps, on the basis of effective and discrete laminates**

The sized model is subsequently post-processed using *MSC Patran* in order to double check the analytical methods of *HyperSizer* by numerical ones.

**4 Structural proof**

The verification of structural integrity is done primarily by numerical analysis. The basis for the analyses is a finite element model of the full aircraft with higher detail than the sizing model. Element stresses are computed by static and dynamic analyses in order to check failure criteria of composite or maximum allowable stresses for metallic parts. Further, the static stability of the structure is ensured by linear buckling and geometrically nonlinear static analysis.

Additionally, an experimental component test of a manufactured rib is carried out, in order to verify analysis and material strength.

#### 4.1 Verification by detailed numerical analysis

The starting point for the FEM analysis of the full aircraft is the detailed 3D geometry model including all individual composite and metallic parts of the primary structure and control surfaces (cf. Figure 1). Shell elements are chosen predominantly in the FEM discretization. Adhesive joints are modelled by solid layers, connected to the shell elements of the bonding partners. Bolted joints, respectively are represented by bar elements. Non-structural masses, such as equipment, fuel, paint, etc. are included by concentrated mass elements, whose inertial loads are distributed to the structure by 1D RBE3 elements. The element size varies from 5 mm to 10 mm, amounting to about 1 million elements for the complete model.

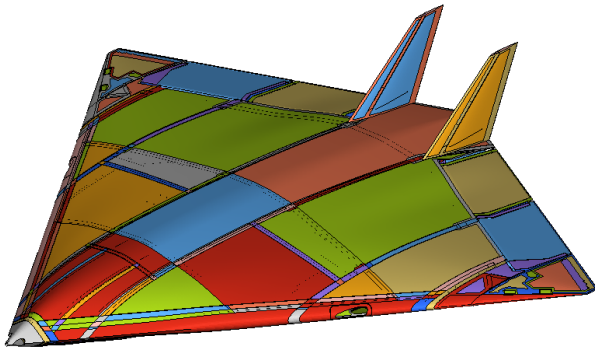


Figure 8: Finite element model for structural proof with individual colours for separate property sections

The landing gear is simplified by *CBAR* bar elements. External landing loads are introduced at one load transfer point for each landing gear.

##### 4.1.1 Stress proof

For composite parts, the *Tsai-Wu* failure criterion is selected. The maximum ply failure index must be less than unity even when Ultimate Loads are considered.

$$FI = \sigma_1 \left( \frac{1}{X_T} - \frac{1}{X_C} \right) + \sigma_2 \left( \frac{1}{Y_T} - \frac{1}{Y_C} \right) + \frac{\sigma_1^2}{X_T X_C} + \frac{\sigma_2^2}{Y_T Y_C} - \frac{\sigma_1 \sigma_2}{\sqrt{X_T X_C Y_T Y_C}} + \frac{\tau_{12}^2}{S^2} \quad (3)$$

Where  $\sigma_1, \sigma_2$  and  $\tau_{12}$  are in-plane normal and shear stresses,  $X_T, X_C, Y_T, Y_C$  are the ply tensile/compressive allowable stress in fibre-parallel and fibre-perpendicular direction.  $S$  is the ply shear allowable stress.

For all static load cases, an envelope of maximum element failure index is created and reviewed. Figure 9 shows a contour plot of the failure index for internal composite parts (landing gear ribs) at landing loads. In the load introduction areas of the landing gear, local failure

indices exceed the allowable. However, it is assumed that the landing gear loads are not correctly distributed to the structure by the simplified attachment modelling. The proof for the landing gear ribs is thus performed by the evaluation of bearing stresses. Similar scenario also occurs at the detachable vertical twin tail. Screw cut-outs show critical failure indices but the respective bearing stress is within allowable limit. The required detachability of the twin tail forbids the use of permanent bonding which would remedy stress concentration around the holes.

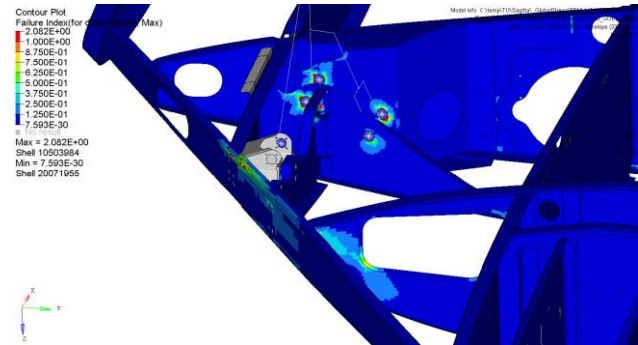


Figure 9: Failure Index of internal parts at landing loads

##### 4.1.2 Proof of adhesive joints

The massive usage of load-bearing composite components demands sufficient joining technologies to take advantage of their lightweight capabilities. From a mechanical perspective, adhesive bonding is the favourable joining technique as thin-walled parts could be joined and material weakening due to holes and subsequent local stress concentrations is avoided.

Although being very competitive compared to other joining technologies, some challenges arise if adhesive bonding is used. Advanced and efficient design methodologies are still subject of research and scientific discussions. As the majority of structural components of *Sagitta* are adhesively bonded, attention is directed to a newly developed semi-analytical design criterion for bonded joints (see Section 4.2.2). As part of this new method, determination of both, adhesive material data and joints strength for different loading conditions is needed and thus briefly discussed.

##### Adhesive material selection

Adhesive selection is based on a list of mandatory requirements that needs to be met. With their mechanical and physical properties, epoxy adhesives are most suitable for combination with likewise epoxy-based CFRP structures. Thus, epoxies are the most relevant structural adhesives used and could be seen as standard material of choice for structural bonds. Among available adhesive systems, following properties are highly desirable for *Sagitta*:

- high shear strength ( $> 20 \text{ MPa}$  at  $T_{max}$ )
- high peel strength
- high temperature resistance
- low E-modulus ( $< 3.0 \text{ GPa}$ )

- high resistance to harsh environments and chemicals
- paste-like processing at room temperature
- thixotropic characteristics

Three eligible adhesive systems have been identified. Selection is made after comparing their shear strength experimentally. Based on those results and supported by further existing experiences with the adhesives, 3M™ Scotch-Weld™-9323 B/A is selected as material of choice. Moreover, this adhesive is Airbus certified and therefore applicable for aeronautical applications. The adhesive material is subsequently by means of several methods as depicted in Table 2:

**Table 2: Adhesive test matrix**

Property	Test method
Young's modulus	Dynamic Mechanical Analysis (DMA) [4]
Shear strength	Single Lap Shear (SLS) test [5]
Peel strength	Single L-Joint test

### Young's modulus and characteristic temperature

The Young's modulus is obtained by DMA and amounts to 2.53 GPa. The onset for stiffness degradation is detected at  $T = 53.72$  °C. The Poisson's ratio of  $\nu = 0.39$  is used. In order to fulfil the temperature requirements for the structure the loss of stiffness and strength has to be considered in the following.

### Shear strength

Figure 10 depicts the shear strength test specimen, its manufacturing, the typical stress distribution in the adhesive layer and the fracture pattern. The resulting value from this investigation is the virtual maximum shear strength of the adhesive system. As this parameter also involves the appearance of fracture in the adherents, it is no pure adhesive-specific value. The deduced constant is further adjusted for reasons of probability (B-Value) and for its temperature-dependent characteristic.

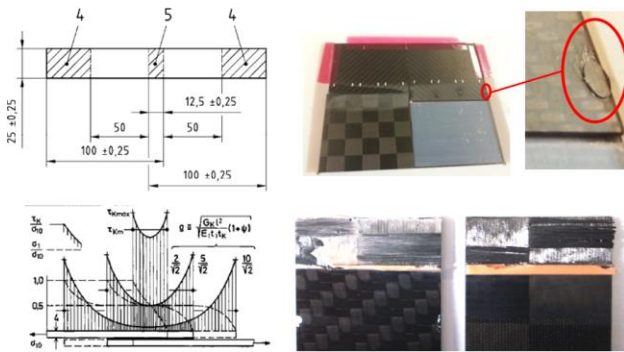


**Figure 10: Experimental setup [5] and stress distribution [6] for single lap shear test (left), specimen manufacturing (top right) and fracture pattern (bottom right)**

A parameter study is processed to examine the effects of varying joining members and adhesive thicknesses on the strength of the joint. The minimum average shear strength of  $\tau_{m,avg} = 21.09$  MPa results for a combination of adherents which are both built from T800, MTM49-3 fabric. With a standard deviation of 2.487 and a tolerance

limit factor of  $k_b = 1.282$ , the shear strength reduces by 15.1 % to its B-value  $\tau_{m,B} = 17.89$  MPa.

The shear strength is further reduced for the consideration of temperature dependent degradation according to datasheet values. The final adhesive mean shear strength amounts to  $\tau_{m,B,T} = 12.68$  MPa, what corresponds to a percentage reduction of the  $\tau_{m,avg}$  value of 39.9 %. According to [6] the maximum shear strength  $\tau_{k,max,B,T}$  within the adhesive is calculated with

$$\tau_{k,max,B,T} = \tau_{m,B,T} \frac{\rho}{2} \left[ \coth \frac{\rho}{2} + \frac{1-\psi}{1+\psi} \tanh \frac{\rho}{2} \right] \quad (4)$$

to  $\tau_{k,max,B,T} = 18.74$  MPa. The bonding coefficient  $\rho$  and the adherent thickness ratio  $\psi$  are calculated dependent to the loading condition (for further details see [6]). The maximum cohesive load per width  $p$  [N/mm] used for the dimensioning of glued joints is computed for single-L-joints with

$$p_{m,B,T,SL} = \frac{\tau_{k,max,B,T}}{\rho \coth \rho} * l \quad (5)$$

and for double-L-joints with

$$p_{m,B,T,DL} = \frac{\tau_{k,max,B,T}}{\frac{\rho}{2} \left[ \coth \frac{\rho}{2} + \frac{1-\psi}{1+\psi} \tanh \frac{\rho}{2} \right]} * l \quad (6)$$

and results in  $p_{m,B,T,SL} = 31.27 \frac{N}{mm}$  and  $p_{m,B,T,DL} = 83.38 \frac{N}{mm}$  for the maximum beneficial bearing flange length  $l = l^*$ . The adhesive single- and double-L-joint, which is loaded with a maximum shear line load  $p_{max}$  can withstand shear forces when

$$(p_{m,B,T}/p_{max}) - 1 > 0. \quad (7)$$

The L-shaped geometry of the flanges reduces manufacturing complexity. With the resulting values from equations (5) and (6), an increase of strength for double-compared to single-L-joints of 266 % can be found. Due to the increased bending momentums and the short maximum bearing length  $l^*$  of the flange, the negative effects of a single-L-joint on the peel strength are of the same magnitude. Experimental and simulative investigations evaluate this correlation.

### Peel strength

The second load type of adhesive joints is characterized by peel stresses. Following existing testing standards [7] and publications regarding CFRP single L-joint bonding [8], a test setup is designed and numerically evaluated which allows to determine the maximum bearable line load of an adhesive joint (cf. Figure 11).

The geometry of the adhesive spew is identified by FEM computations to have significant influence on the strength of a bonded peel-stressed joint. Based on a numerical preselection of concepts, three different geometries for the adhesive spew are tested. Additional values for the double-L-joint configuration with post-bonding integrated



brackets in a wet laminate process are measured. For *Sagitta* the single-L-joint with a chamfer-shaped spew is used for lightly loaded joints and wet-laminate-reinforced double-L-joint is utilized where huge forces have to be born. The resulting values are further processed equally to the shear strength values.

The peel strength of a bonded single-L-joint is  $q_{B,T,SL} = 25.19 \frac{N}{mm}$ , with a reduction compared to the initial average strength of 42.6 %, considering B-Value and temperature aspects. The peel strength of a bonded double-L-joint, like depicted in Figure 11, middle, is  $q_{B,T,DL} = 67.36 \frac{N}{mm}$ , with a reduction compared to the initial average strength of 38.3%.

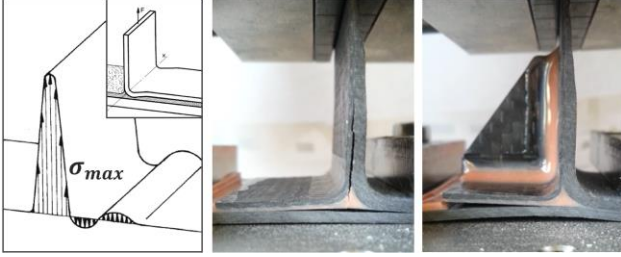


**Figure 11: Typical L-joint peel stress distribution (left) [9] and fracture pattern for wet-laminate-reinforced double-L-joints without (middle) and with (right) flange support**

The design proof criteria for the maximum peel line load  $q_{max}$  is given by

$$(q_{B,T}/q_{max}) - 1 > 0. \quad (8)$$

Shear and peel loads cannot be analysed separately. The allowable loads for the directional components of a superimposed load state lie below the tested values for single load direction. To provide a remedy, the proof criterion considers load combination. A quadratic approach is used to compute the strength of the joint design:

$$1/\sqrt{\frac{1}{SF_{SHEAR}^2} + \frac{1}{SF_{PEEL}^2}} - 1 = 1/\sqrt{\left(\frac{p_{max}}{p_{m,B,T}}\right)^2 + \left(\frac{q_{max}}{q_{B,T}}\right)^2} - 1 > 0. \quad (9)$$

$SF_{SHEAR}$  and  $SF_{PEEL}$  are the safety factors for shear and peel loads in a separated analysis of adhesive joint load types.

### Load analysis

Adhesive joints are modelled in the design proof FEM-model with 3D elements. The stiffness influence of the adhesive film is thus included in the computation. For the detailed analysis of bonding stresses a semi-analytical strategy is developed, which bases on the investigation of element forces. Figure 12 visualizes the extraction of element forces from web and flange elements of the global design proof model at the example of a highly

loaded landing gear rib. The occurring loads on the adhesively bonded flange can be divided into five major stress cases. The web elements hold the information about

- shear stress,
- tensile stress (not considered) and
- peel stress.

Stress types that can be extracted from flange elements and for which the adhesive joint serves as patch are

- base shear stress (not considered) and
- base tensile stress (not considered).

Shear and peel stresses are extracted from the flange nearest web elements and are used for the subsequent bonding analysis. Flange-parallel tensile stresses are minimal, because of an approximately perpendicular connection to the web. Base stresses from the subjacent joint member are investigated. It is found that the resulting adhesive loads are orders of magnitude below web loads and do not influence the design of the adhesive joint for the given structural application. Together with the characteristic parameters for the adhesive joint, the reliability of the connection design is evaluated. The specifically developed design tool lists the resulting safety factors for each component, every load case and additionally names the most stressed element.

The evidence for all adhesive joints is provided by using either single- or double-L-joint connections, depending on the occurring loads.

### 4.1.3 Proof of bolts

The utilized joint elements are divided into two groups, fasteners and bolts. Fasteners are applied to mount electronic equipment, sensors, like cameras and actuators and include small rivets, metal clips and plastic elements. Bolts are used to realize highly loaded structural joints and are needed to connect the attachments of termination system and landing gear with the airframe.

The fastener strength values are deduced experimentally in a shear [10] and a pull-trough [11] test. Therefore a pulling strap is mounted with the examined fastener to a CFRP plate with representative layup (thickness 0.88mm; material T800, MTM49-3) and bearing, which are slightly modified compared to the given test standard to enhance comparability (cf. Figure 13, top). The obtained fracture loads together with the simulated stresses are used to verify structural integrity. A fastener element is applicable when

$$(X_{F,\parallel}/F_{F,\parallel}) - 1 > 0 \text{ and} \quad (10)$$

$$(X_{F,\perp}/F_{F,\perp}) - 1 > 0. \quad (11)$$

The occurring structure parallel and perpendicular fastener forces  $F_{F,\parallel}$  and  $F_{F,\perp}$  must be less than the measured shear force  $X_{F,\parallel}$  and the pull trough-force  $X_{F,\perp}$ .

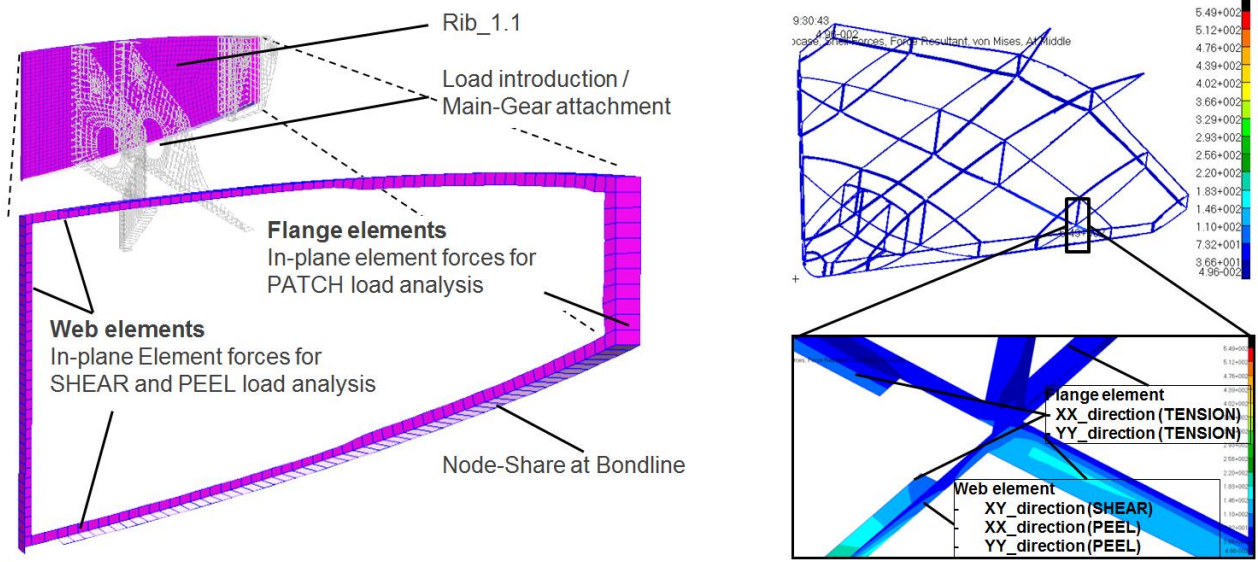


Figure 12: Extraction of element forces as input for semi-analytical approach for adhesive joint design

The tolerable stresses for the termination system joints are of major interest. Hole bearing specimens are experimentally tested according to DIN 65562 [12] in order to determine the bolts' characteristic value, tensile force per specimen thickness and hole diameter (see Figure 13). Eight specimens with the dimensions of  $90 \times 40 \times 1.98 \text{ mm}^3$  are tested, in order to treat B-Value reductions. The specimen material is equal to the material used for the inner structure, T800, MTM49-3. The laminate layup  $[+45,0,+45,0,+45,0,+45,0,+45]$  is used. The measured test data, showed a typical course of force over crosshead travel. Though the first decrease of loads indicates fracture and provides the input value for the dimensioning of bolted joints, an increase of testing force to the double can be observed for a crosshead travel of up to  $6 \text{ mm}$ . The force value at the first event is extracted for the computation of the hole bearing strength  $\sigma_{HB,B}$  of a joint. Considering B-Value reduction, a fracture load of  $F_{HB,B} = 3.202 \text{ kN}$  results, which leads to  $\sigma_{HB,B} = 202.16 \text{ MPa}$ . A joint with hole diameter  $d_B$  and structural thickness  $t_{CFRP}$  can withstand the applied structure parallel forces  $F_{B,\parallel}$ , when

$$(\sigma_{HB,B} d_B t_{CFRP} / F_{B,\parallel}) - 1 > 0. \quad (12)$$

Stresses due to structure perpendicular forces are evaluated for the airframe structure, the bolt and the attachment. Failure due to pull through has to be avoided by sufficient dimensions of the support area.

According to the allowable bearing stress  $\sigma_{HB,B}$ , the maximum shear force for each fastener is retrieved from linear-static FE analysis for the given design load cases as defined in Chapter 2.1. For landing load cases and bolts with  $d_B = 3 \text{ mm}$ , the shear stress at several skin covers exceeds the limit value for bearing stress of  $\sigma_{HB,B}$ . However, the averaging shear force per fastener row results in stresses that can be covered with the conceived bolt diameter and thus complies the bearing stress criteria. Although, stereo camera covers experience high shear forces at the some locations, their laminate is almost two times thicker than other covers. Subsequent maximum bearing stress is within the limit. Overall M3 fasteners' shear and tensile forces obtained from landing loadcases are plotted in Figure 14 and Figure 15.

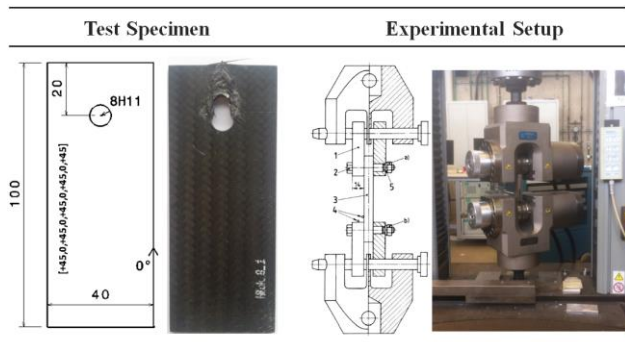


Figure 13: Test specimen and experimental setup for bolted joints with diameter  $d=8 \text{ mm}$  and CFRP specimen thickness of  $t=1.98 \text{ mm}$

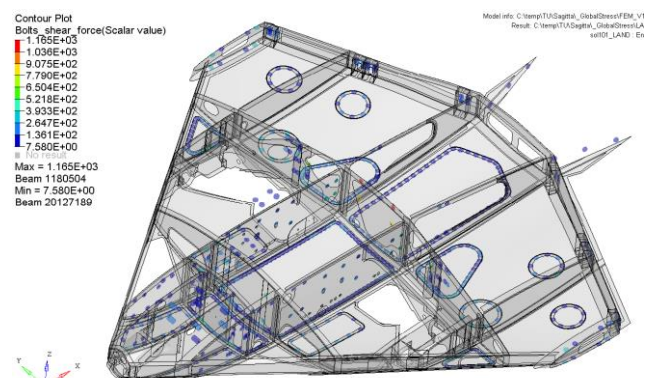


Figure 14: Maximum shear force plot for bolts of  $d_B = 3 \text{ mm}$  and landing load envelope

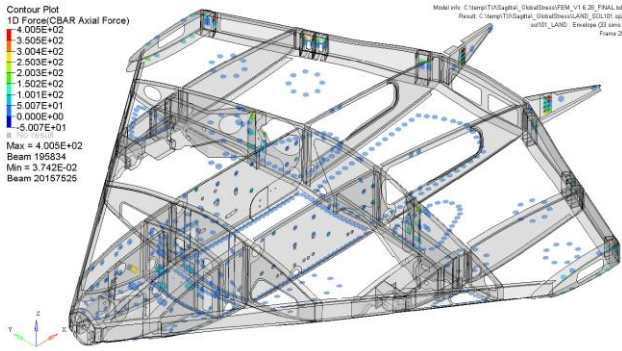


Figure 15: Maximum axial force plot for bolts of  $d_B = 3 \text{ mm}$  and landing load envelope

#### 4.1.4 Buckling proof

The proof of the aircraft's structural stability takes all static and quasi-static load cases into account. First, linear buckling analysis is processed. Corresponding linear buckling factors are evaluated for ultimate load level. A structure is stable when

$$\lambda - 1 > 0. \quad (13)$$

is fulfilled. In the event of occurring critical buckling factors ( $\lambda < 1$ ), a geometrical nonlinear analysis via quasi-static loads is applied to examine geometrical stability in the post-buckling regime. With a minimum linear buckling factor of 0.16, landing loads turned out to be the most critical load cases, as shown in Figure 16. However, nonlinear geometrical analysis proved that those early buckles confine to local corners around cut-outs, and no structural instability is expected for Ultimate Load levels (see Figure 17).

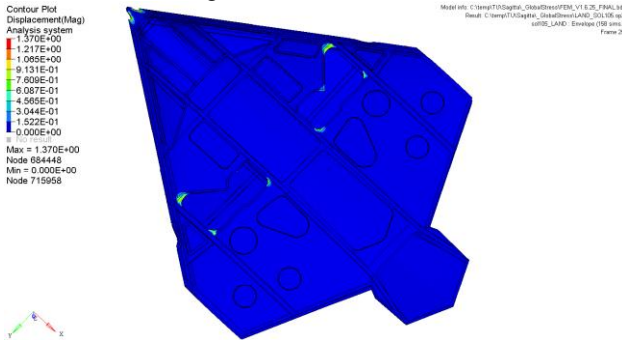


Figure 16: Critical buckling mode envelope for landing loads,  $\lambda = 0.16 \dots 1.15$

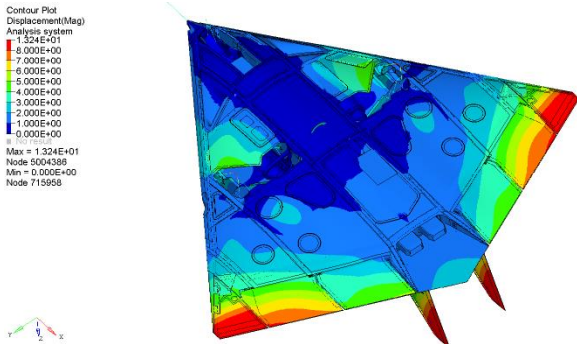


Figure 17: Displacement envelope plot for landing loads from nonlinear analysis

#### 4.1.5 Aeroelastic stability

Static and dynamic in flight aeroelastic stability, like divergence, control reversal and flutter, has to be proven according to the certification specifications CS-23.

Structural damping is assumed to be 0.020 and constant over frequency. This assumption is justified, by the use of foam cores in the sandwich panels, as well as the application of structural bonds, rather than monolithic parts. The results of the flutter analysis are shown in terms of damping ratio of the eigenvalues of the aeroelastic system over air speed. Up to an air speed of  $v = 120 \text{ m/s}$  at sea level, no flutter mode exceeds zero damping value (cf. Figure 18). Thus, the aircraft is considered flutter-free as its maximum flight speed is  $v_{max} = 100 \text{ m/s}$ .

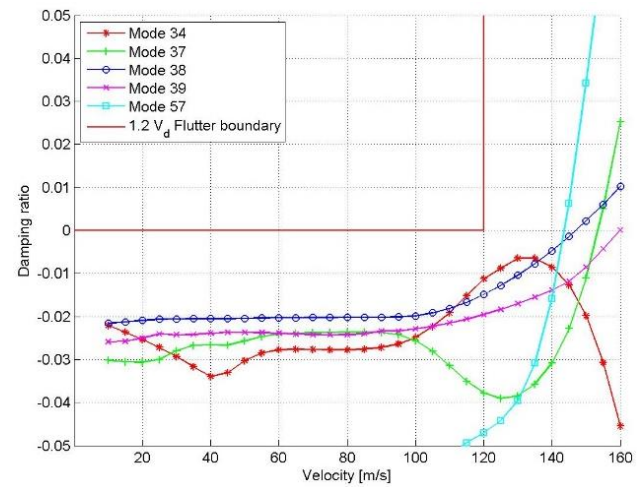


Figure 18: Aeroelastic modal damping vs. air speed

The most critical flutter modes mainly involve the vertical tail, outboard flaps and skin fields. Flutter modes 34 and 57 are the closest to the minimum flutter speed  $1.2v_{max}$  as derived from Figure 18. The antisymmetric aeroelastic flutter mode shape is shown exemplarily for mode 34 in Figure 19.

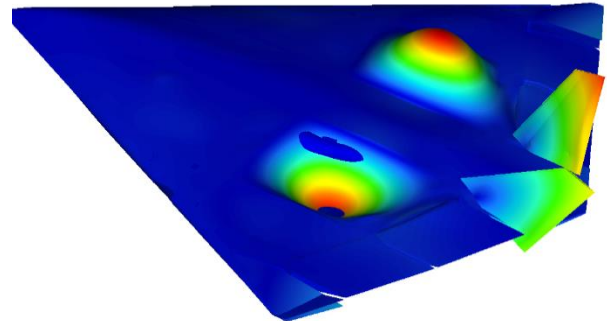


Figure 19: Aeroelastic mode shape 34

## 4.2 Verification by structural component test

In order to verify the simulation results and thereby evaluate the software and design procedure using *MSC Nastran*, a single component is manufactured for physical testing. First the accordance of the linear elastic behaviour of experiment and numerical computation is verified. The examination of the fracture load is done in a subsequent step. The selected component for the experimental test has to

- be a structural important and highly stressed component,
- possess a representative laminate layup,
- ensure that the achievable loads result in strains high enough to be measured accurately ( $\epsilon > 1e - 4$ ) and with only moderate gradients in highly stressed regions,
- possess a geometry with flat regions, which can be born reliable and without local overloads and
- be of a size, that is conform with the testing capabilities at DLR Braunschweig.

The selected test specimen, which fulfils these demands, is Rib1.1\_1. The measuring equipment allows to record local strains in two ways during the test procedure. Punctual strains, marked in Figure 20 with crosses, are measured with strain gauges whereas areal strain information is logged by the 3D camera system *GOM Aramis*. The related test forces from the testing machine are overlaid to be able to compare numerical and experimental results.

The results of the linear elastic investigations lead to the following conclusions:

- Higher strains in FEM data indicate too small material values within the FEM simulation for tension, compression and shear stiffness.
- The elastic behaviour of FEM model and experimental setup is nearly identical and linear but shows different slopes (see Figure 20).
- Deviations up to 60% occur for low load levels, due to manufacturing accuracy near transitions to rib flanges and sandwich structures.

Besides the local strain values, the most important parameter for the evaluation of the numerical design process is the fracture load. The fracture load was evaluated as the force of the first event, where the test forces first decreases for increasing crosshead travel. The test specimen, component Rib\_1.1\_1, withstands and exceeds the predicted fracture loads. The fracture loads lie between +68% and +138% higher than the simulated values. These deviations can mainly be explained with the applied correction factors that are applied to the material constants and in addition with geometrical inaccuracies at the critical area near the bearing of the specimens.

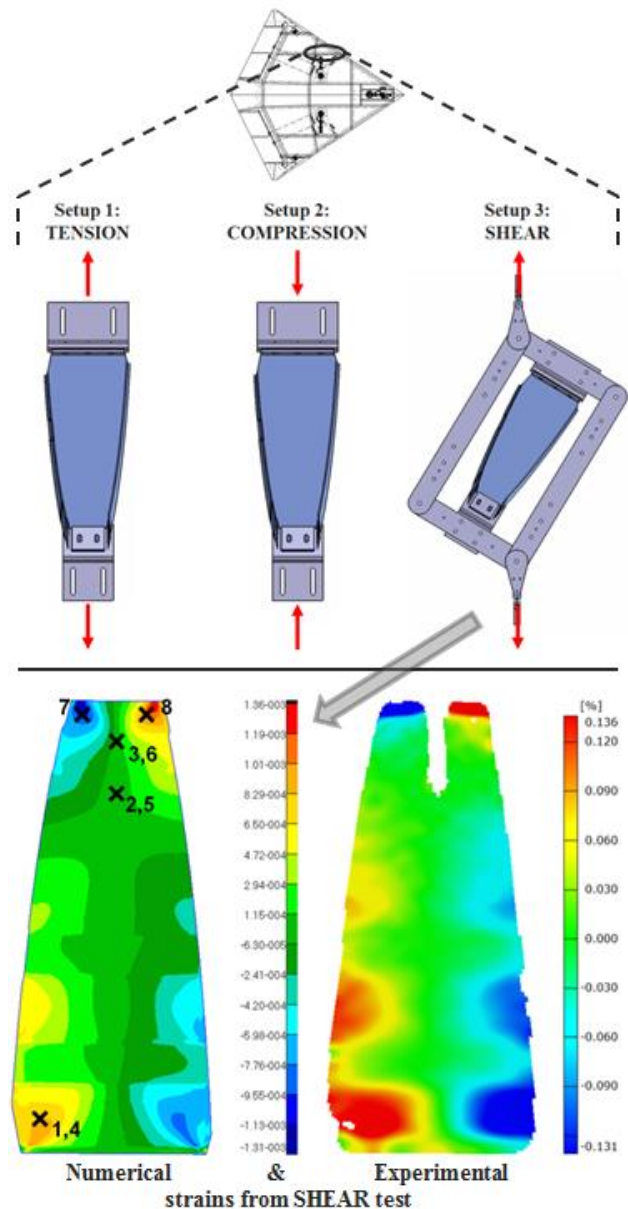


Figure 20: Experimental setup and comparison of strains from numerical and experimental investigations

Figure 21 summarizes the fracture loads that are predicted by simulations and measured in physical test.

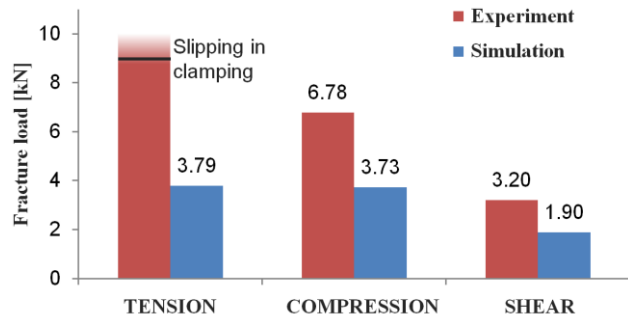
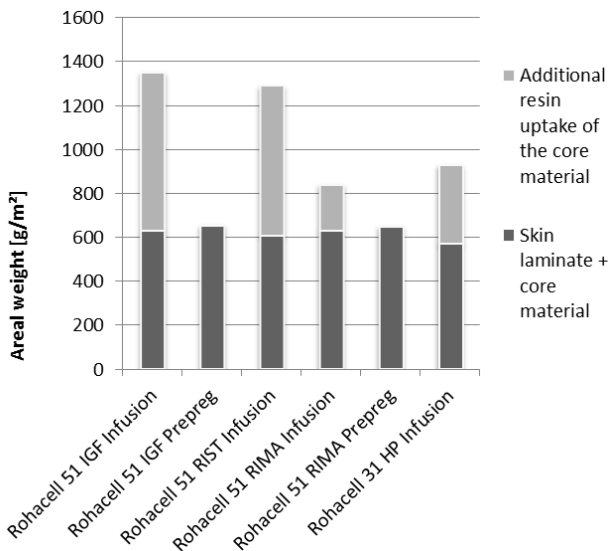


Figure 21: Comparison of experimental and numerical fracture loads of structural test specimen

## 5 Manufacturing

### 5.1 Manufacturing of upper and lower shell

The main aim during the preparation process for the manufacturing of both skins of the *Sagitta* demonstrator is to keep the areal weight of the shell material as low as possible. This is particularly important as the chosen flying wing configuration results in an overall surface area of approximately nine square meters. Therefore it is necessary to reach an average areal weight below  $1 \text{ kg/m}^2$  to be able to meet the target weight of  $30 \text{ kg}$  for the assembled airframe including lids and flaps. Preliminary manufacturing tests show that the resin uptake of the core material surface is the weight component that has to be reduced. To perform comparability, an exemplary stack-up sequence is determined for manufacturing tests, which is based on the preliminary sizing results. It is symmetrical and consists of two skin layers of *Textreme* prepreg with an aerial weight of  $80 \text{ g/m}^2$ , 48 % resin weight portion on each side and a  $2 \text{ mm}$  core layer. The following table shows the areal weight of test specimens that were manufactured using the different *Rohacell* core materials that are introduced in chapter 3.1.1.3. Figure 22 shows that a resin infusion process leads to a tremendous increase of the resin uptake of the core surface. The best result using a resin infusion process can be achieved with the *Rohacell RIMA* core material. Its fine pored surface leads to an additional weight of  $200 \text{ g/m}^2$  compared to the specimen manufactured from prepreg.



**Figure 22: Minimum areal weight of an exemplary stack-up depending on core material and manufacturing process.**

Comparing specimen two and specimen five which are both made from prepreg it can be seen that there is no difference in the overall areal weight despite the fact that the *Rohacell IGF* has larger pores than the *Rohacell*

*RIMA* foam. Figure 23 shows a cross section of both specimens.

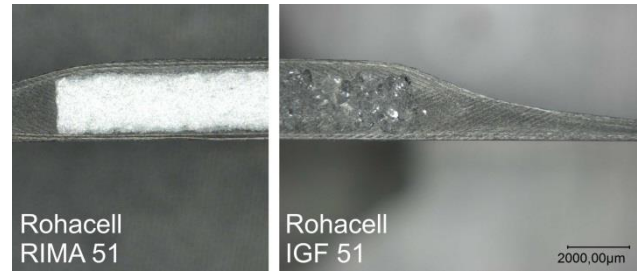


**Figure 23: Cross section of the exemplary laminate showing the different porosities of *Rohacell RIMA* and *Rohacell IGF***

There occurred one major drawback using a large pored foam core with thin skin layers made from prepreg. Depending on the resin weight of the prepreg and the stack-up the skin laminate may lack resin because of the resin uptake of the core. This results in an imperfect impregnation of the skin laminate. For this reason the *Rohacell RIMA* foam is chosen as core material for the shells of the *Sagitta* demonstrator.

To reduce manufacturing time and tooling costs both shells are processed in just one step and in one single tooling including all skin reinforcements, covers and doors. Figure 24 shows one of the integrally manufactured maintenance covers of the lower skin. To do so the plies of the covers and lids are cut net-shape and preformed with their individual foam core. These preforms are the first in the laminating process to be put into the mould. One layer of peel ply between covers and surrounding skin laminate ensures that they can be separated after the curing process.



**Figure 24: Integrally manufactured cover of the *Sagitta* lower skin**

As a drawback this totally integral approach leads to extensive stack-up sequences for both skins. The lower skin consists of 213 plies. The ply table of the upper skin counts 336 single plies. For a proper positioning inside the mould and especially of the door preforms, a laser projector is mandatory. For weight and therefore handling reasons and due to the low thermal expansion compared to aluminium the shell tooling is also made of CFRP. The curing process took place in an autoclave at up to  $100^\circ\text{C}$  and 5 bar absolute pressure. Both, higher pressure and higher temperature would improve the quality of the CFRP laminate but it would also cause the foam core to collapse during the process due to its limited strength.



Figure 25: *Sagitta* lower skin in the CFRP tooling after the curing process, covered with the vacuum bagging.

Figure 25 depicts the lower skin inside the CFRP shell tooling after the autoclave curing. It also shows the large number of covers and doors that are manufactured in the same step. One can see in the picture that there is very little breather used for the vacuum bagging. The reason is that in fact all surplus resin of the skin plies is necessary for the interface to the core material. Therefore excessive bleeding must be prevented.

## 5.2 Manufacturing of the inner structure

Unlike the shells of the *Sagitta* demonstrator which are made from *TeXtreme* spread tow fabric the inner structure is made from a regular carbon fibre 2x2 twill fabric prepreg. The resin system is *Cytec* MTM49-3 with a resin weight of 42 % and an areal weight of the fabric of  $200 \text{ g/m}^2$ . This material is chosen because of the lack of drapability of the *TeXtreme* fabric especially in narrow moulds. A second reason is that packaging and preliminary design showed that there have to be hard points on each of the ribs and spars. This means that a higher wall thickness is preferable to deal with the bearing stresses at those points. In this case the *Textreme* fabric loses its main advantage which is the ability to manufacture extremely thin laminates. *Rohacell RIMA* is chosen as core material due to the findings concerning the lower resin uptake during the manufacturing of the shells.

The huge number of individual parts and the resulting effort lead to a reassessment of the manufacturing process. To simplify tooling manufacturing and preproduction of the components of the inner structure they all do have a c-shape cross section with a draft angle at the flanges. This enabled the milling of simple flat moulds. The surrounding flange with the draft angle and the reinforced web with the cut-outs for the air intakes are shown at the exemplary component Spar 1 in Figure 26. One drawback of the board material is the huge thermal expansion of about  $40 \cdot 10^{-6} \text{ K}^{-1}$  and the related distortions that occur even at curing temperatures of about  $80 \text{ }^\circ\text{C}$ . Results from preliminary manufacturing tests on this board material showed that it has to be coated with paint or resin or sealed with PTFE-film to reduce the surface roughness of these moulds.



Figure 26: Spar 1 with cut-outs for the jet engine intakes, enlarged cross section of the sandwich area

Figure 27 shows a microscopic view 500 x enlarged on the surface of a specimen which was manufactured in a mould milled from board material. The tooling was sealed using regular release agent. It depicts the large amount of dimples with a depth of approximately  $0.03 \text{ mm}$ .

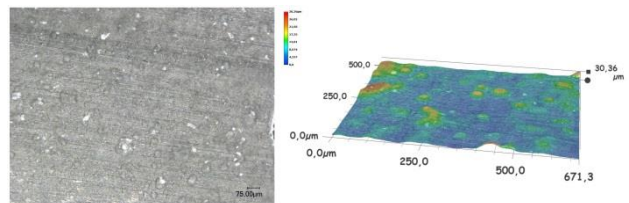


Figure 27: 500x enlarged microscopic view on the surface of a CFRP part manufactured in a mould made from board material

Demoulding of the parts is feasible but the surface roughness inhibits the sliding of the plies in the mould. As the tooling expands during the autoclave curing, the plies peel off in areas of bends or small radii. A minimum surface roughness for example by using a PTFE-coating prevents this effect. Metal tooling for example made from aluminium does have a lower thermal expansion and a lower surface roughness but the costs per tooling are significantly higher compared to the board material. To avoid bridging through the vacuum bagging in the transition from web to flange neither peel ply nor breather is applied in those areas. All components were autoclave cured at  $100^\circ\text{C}$  and 5 bar absolute pressure.



**Figure 28: Roll-out of *Sagitta* after structural assembly at the DLR in Brunswick (top, bottom middle, bottom right), *Sagitta* at ILA2014, Berlin (bottom left) [13]**

### 5.3 Assembly and integration

Depending on the results of the stress calculation structural bonding and bolting are applied to assemble the demonstrator structure. As almost all adhesive joints are crucial and control of success for adhesive bonds is limited, bonding processes call for special care. All bonding surfaces are grinded thoroughly but carefully prior bonding. Cleanliness of bonding surfaces is subsequently controlled by means of a water break test. Adhesive mixing is done in a speed mixer with predefined parameters to ensure homogenous adhesive properties. The adhesive is applied manually out of a cartridge. Novel designed surface distance features are implemented in low loaded areas within the bondline to guarantee a minimum bond line thickness. Hence, kissing bonds as local bond areas with insufficient or even without adhesive are avoided.

In the first step the leading edge spars are bonded to the upper skin. After that the assembly sequence goes on with spar 0 in the front along the x-axis of the airframe up to the rear spar. The last step of the sequence is closing the flying wing by applying the second shell. This is particularly demanding as there are only some small openings that can be used for inspection of the bonding or for rework. To ensure the accurate aerodynamic shape a spare CFRP-mould is used to support the upper skin during the assembly process. This support is levelled and aligned to a 3D workbench using 3D measuring equipment. As the workbench serves as a reference during the assembly this alignment also ensures the ability to

position all spars and ribs accurately. Figure 29 shows the *Sagitta* assembly rig including the support and the 3D workbench. The components of the inner structure are placed on the upper skin for a preliminary fitting test.



**Figure 29: Assembly rig of the *Sagitta* demonstrator, preliminary fitting of the inner structure with the upper shell**

The availability of major components or at least of dummies for example of the landing gear, the fuel tank and the jet engines including all ducts is important for the assembly. The same applies to the whole wiring harness. The integration of those critical components in this early phase of the assembly process makes sure that the components fit and work properly later on.

## 6 Conclusion

The structure of the *Sagitta* demonstrator is successfully designed, proofed by analysis and experimental tests and finally manufactured. The weight of the structure including control surfaces, vertical tail, heatshield and varnish ended up to approximately 36 kg and amounts to one quarter of the maximum take-off weight. The structural analysis evaluates the critical parts for the different loading conditions.

The most challenging design issues, which had to be overcome, are identified as the dimensioning of adhesive joints and the design of the landing gear attachments. A novel semi-analytical method for dimensioning adhesive joints is developed, which compares the experimentally determined strength values analytically with loads that are extracted from the global FEM model. The reliable dimensioning of adhesive joints is thus enabled. Landing loads have turned out to significantly exceed the expected values, which are determined during preliminary analysis. Structural modifications had to be applied to better distribute loads and thus relief the landing gear attachments and further the related adhesive joints.

With the successful structural proof, the manufacturing and assembly, the *Sagitta* structure is ready for integration and flight test.

The UAV structure is assembled and completed for the integration phase, in March 2015. In the following the flight hardware, like landing gear, fuel tank, electronic components with power supply, actuators and flight control units are installed and tested. First flights of *Sagitta* are scheduled for spring 2016.

## 7 Acknowledgments

Airbus Defence and Space supports the project *Sagitta* with resources and large expertise. The productive cooperation with the participating research institutes allowed handling and overcoming even complex and interdisciplinary issues. The excellent teamwork and support is gratefully acknowledged.

## 8 Literature

- [1] Hövelmann A. et al.. Experimental investigations on vortex flow phenomena of a diamond wing configuration. In 29th Congress of the International Council of the Aeronautical Sciences, ICAS 2014; 2014; St. Petersburg, Russia. Code 108502.
- [2] Frey A. et al.. Überwachungsinstanz zur Trennung des Missionssystems und des Flugkontrollsystems in dem unbemannten Luftfahrtsystem SAGITTA. In Deutscher Luft- und Raumfahrtkongress 2014; 2014; Augsburg, Germany. urn:nbn:de:101:1-2014121216572.
- [3] Collier Research Corporation. HyperSizer methods and equations documentation. 2004..
- [4] Normenausschuss Kunststoffe. Bestimmung dynamisch-mechanischer Eigenschaften. Deutsche Norm. Berlin, Germany: Deutsches Institut für Normung e.V., Kunststoffe; 2011. Report No.: DIN EN ISO 6721.
- [5] Normenausschuss Materialprüfung. Bestimmung der Zugscherfestigkeit von Überlappungsklebung. Deutsche Norm. Berlin, Germany: Deutsches Institut für Normung e.V., Klebstoffe; 2009. Report No.: DIN EN 1465.
- [6] Wiedemann J.. Leichtbau, Elemente und Konstruktion. 3rd ed. Berlin: Springer Verlag; 2007.
- [7] Normenausschuss Materialprüfung. Klebstoffe - Bestimmung des Schälwiderstandes von Klebungen. Deutsche Norm. Berlin, Germany: Deutsches Institut für Normung e.V., Klebstoffe; 1995. Report No.: DIN EN 1464.
- [8] Feih S. et al.. Adhesive and composite failure prediction of single-L joint structures under tensile loading. International Journal of Adhesion and Adhesives. 2005 February: 47 - 59.
- [9] Habenicht G.. Kleben: Grundlagen, Technologien, Anwendungen. 5th ed. Berlin: Springer Verlag; 2006.
- [10] Airbus. Fiber reinforced plastics - Determination of joint strength of mechanically fastened joints. Airbus Test Method. Blagnac, France:, Airbus S.A.S Engineering directorate; 2009. Report No.: AITM 1-0065.
- [11] Airbus. Fibre reinforced plastics - Determination of pull-through strength of mechanical joints. Airbus Test Method. Blagnac, France:, Airbus S.A.S Engineering directorate; 2011. Report No.: AITM 1-0066.
- [12] Normenstelle Luftfahrt. Prüfung von multidirektionalen Laminaten, Bestimmung der Lochleibungsfestigkeit. Deutsche Norm. Berlin, Germany: Deutsches Institut für Normung e.V., Faserverstärkte Kunststoffe; 1991. Report No.: DIN 65562.
- [13] AIRBUS Group. Airbus Group - *Sagitta*: Airbus Defence and Space open collaboration project. [Online].; 2015 [cited 2015 August 13. Available from: <http://www.airbusgroup.com/int/en/news-media/media~item=jcr%3A3095d1f2-a930-4c90-92b3-087a017f654d~.html>.